

# Non-adiabatic Effect on Convective Mode

Hiroyasu ANDO,<sup>1,2</sup>

<sup>1</sup>National Astronomical Observatory of Japan, National Institutes of Natural Sciences, 2-21-1, Osawa, Mitaka, Tokyo, 181-8588, Japan

<sup>2</sup>Department of Astronomy, Graduate University for Advanced Studies, Shonan Village, Hayama, Kanagawa, 240-0193, Japan

\*E-mail: ando.hr@iris.ocn.ne.jp

## Abstract

The systematic analysis of non-adiabatic effect on convective mode has been conducted using wave energy relation. In the adiabatic analysis, the "propagation diagram" for convective mode is proposed as a useful tool to see its behavior. In the non-adiabatic analysis, it is found that for strongly non-adiabatic case, a monotonically growing convective mode becomes oscillatory. In this phase, the radial displacement and the distribution of wave energy show only one bump, in which the distribution of entropy energy  $e_S$  almost overlaps with the distribution of gravity energy  $e_g$ . Entropy energy  $e_S$  seems to act as potential energy of oscillatory convection. In addition to this, this change occurs not gradually, but abruptly with change of non-adiabatic indicator.

**Keywords:** convective mode – radiative thermal conduction – oscillatory convection – wave energy – solar model

## 1 Introduction

The oscillatory convection was discovered by Shibahashi & Osaki (1981) in the global analysis for highly luminous ( $L = 10^5 L_\odot$ ) stars. In this study, a new type of non-adiabatic unstable modes (called as "A-mode") was found, in which the growth rate (imaginary part of the complex eigenvalue) is comparable with the frequency (real part). So these modes could not be classified as p-, f-, and g-modes. To make clear what kind of mode it is, they performed the numerical experiment for "A-mode", and examined how it changes its behavior by changing non-adiabaticity indicator  $C_2$  in the basic linear equations of non-adiabatic nonradial oscillations (Ando & Osaki 1975). Eventually, "A-mode" was revealed to be a convective mode (i.e.,  $g^-$ -mode) in the adiabatic limit (large  $C_2$ ). They concluded that "A-mode" is an oscillatory convection originated from convective mode. However, they stopped the further systematic study of why and how a convective mode becomes oscillatory due to strong non-adiabaticity. After their work, no systematic study of non-adiabatic effect on convective mode has been conducted, as far as we know.

Three decades later, oscillatory convection was paid an attention to from observational point of view. Saio (2011) and Saio et al. (2015) have proposed oscillatory convection for the explanation of variability in the luminous variable stars. Latter (2016) have also conducted numerical calculations of overstable convection as a dynamical movement in protoplanetary discs.

So far, in the local analysis, Cowling (1957) and Kato (1966) studied the overstability of convective mode under the super-adiabatic medium stabilized by the magnetic fields and by the chemical composition gradient, respectively. But strictly speaking, this kind of instability is different from findings by Shibahashi & Osaki (1981), since the super-adiabatic medium is not stabilized in their situation. The systematic study following their work is, therefore, highly expected.

This paper is devoted to the essential problem of why and how

a convective mode becomes oscillatory with use of wave energy (Eq. 25.12 given in Unno et al. (1989)). The present solar model is used as an equilibrium model throughout this work. In section 2, the basic aspect of adiabatic convective mode is reviewed following the global analysis done by Hart (1973). Then, "propagation diagram" for  $g^-$ -mode similar to that for p-, f-, and g-mode is newly introduced to discuss their features. In section 3, the non-adiabatic analysis of convective mode is developed to understand how a monotonically growing convective mode becomes oscillatory under the thermal conduction through radiation. Section 4 is summary and discussion.

## 2 Adiabatic analysis

As for adiabatic convective mode we use the basic equations for the adiabatic nonradial oscillations given in the Chapter 18 (Eq. 18.14 ~ 18.17) of Unno et al. (1989). The solar model at the present time is calculated as an equilibrium model by Paczyński (1969) program, of which parameters are  $T_e = 5770K$ ,  $R_\odot = 6.96 \times 10^{10}$  cm, the ratio of the mixing length to the pressure scale height  $l/H_p = 2.0$ , chemical composition  $X = 0.7$ ,  $Z = 0.03$ , and the envelope mass  $0.1M_\odot$ .

### 2.1 Propagation diagram

We understand that propagation diagram is a very useful tool to see their trapping region for p-, f-, and g-mode, that is, we can judge how a particular mode of nonradial oscillations behaves in the interior of a stellar model. This diagram is derived from the local dispersion relation of which derivation should consult the paper (Osaki 1975) if necessary. Here the temporal and the spatial variation of perturbations are assumed to be  $\exp(i\sigma t)$  and  $\exp(ik_r r)$ , respectively. The resulting dispersion relation is given by

arXiv:2601.12756v2 [astro-ph.SR] 11 Mar 2026

$$k_r^2 = \frac{(\sigma^2 - L_l^2)(\sigma^2 - N^2)}{\sigma^2 c^2}, \quad (1)$$

where the Lamb frequency and the Brunt-Väisälä frequency are given, respectively in the following,

$$L_l^2 = \frac{\ell(\ell+1)c^2}{r^2}, \quad (2)$$

and

$$N^2 = g \left( \frac{1}{\Gamma_1} \frac{d \ln P}{dr} - \frac{d \ln \rho}{dr} \right), \quad (3)$$

where  $c$  is sound speed, The propagation diagram of the Sun is given in Fig. 1, where characteristic frequencies  $L_l$  and  $N$  are depicted as a function of radial coordinate  $\ln(x/p)$ . In Fig. 1(a), the solar inner core ranges from  $\ln(x/p) = -43.3$  to  $\ln(x/p) = -34.1$ , and its envelope from  $\ln(x/p) = -34.1$  to  $\ln(x/p) = -2.5$ , where  $x$  is fractional radius of the sun ( $r/R_\odot$ ) and  $p$  is pressure.

For a particular mode (given  $\sigma$ ), a corresponding horizontal line in Fig. 1(a) intersects  $L_l$  and/or  $N$  curves. If  $\sigma^2 > L_l^2, N^2$  or  $\sigma^2 < L_l^2, N^2$  in Eq. (1), we obtain  $k_r^2 > 0$  and the solutions of the wave equations in this case present propagating waves. So the propagation diagram (Fig. 1(a)) shows in which portion a particular wave can propagate. In the portion with  $\sigma^2 > L_l^2, N^2$ , a wave has p-mode nature. In case of  $\sigma^2 < L_l^2, N^2$ , a wave has g-mode character. On the other hand, if  $N^2 > \sigma^2 > L_l^2$  or  $L_l^2 > \sigma^2 > N^2$ , we get  $k_r^2 < 0$ . The waves are then non-propagating as a running wave and they are called evanescent waves.

In the case of convective mode,  $\sigma$  is pure imaginary, and so  $\sigma$  is replaced by  $i\sigma_I$  in Eq. (1), which is reduced to

$$k_r^2 = -\frac{(\sigma_I^2 + L_l^2)(\sigma_I^2 + N^2)}{\sigma_I^2 c^2}, \quad (4)$$

In order for  $k_r$  to be real, it should be  $\sigma_I^2 < -N^2$ . This condition is satisfied only in the convective region ( $N^2 < 0$ ). Here we define  $|N| = \sqrt{-N^2}$  and plot it by dashed line in Fig.1(a). As the growth rate  $\sigma_I$  should be below  $|N|$  line, a convective mode is confined in the C-region. Thereafter, we call it as "propagation diagram" for convective mode. Enlarged propagation diagram is shown in Fig.1(b) to see the trapped feature in more detail.

## 2.2 Wave energy

Wave energy is a crucial tool to understand the nature not only of conventional mode, but also of convective mode. The wave energy ( $e_w$ ) per unit mass is given by Eq.(25.12) in Unno et al. (1989) such as,

$$e_w = \frac{1}{2} \left\{ \mathbf{v}^2 + \left( \frac{p'}{\rho c} \right)^2 + \left( \frac{g}{N} \right)^2 \left[ \left( \frac{P'}{\Gamma_1 p} - \frac{\rho'}{\rho} \right)^2 - \frac{\nabla}{\nabla_{ad}} \left( v_T \frac{\delta S}{C_p} \right)^2 \right] \right\}, \quad (5)$$

where  $\nabla$  is temperature gradient ( $d \ln T / d \ln P$ ) and  $\nabla_{ad}$  is adiabatic temperature gradient ( $\partial \ln T / \partial \ln P$ )<sub>S</sub>, and  $v_T = (\partial \ln \rho / \partial \ln T)$ <sub>p</sub> and the other symbols have the usual meanings. The variables with prime and  $\delta$  represent Eulerian and Lagrangian perturbations, respectively.

To proceed further analysis, we transform each term in  $e_w$  into a more convenient form. Using the displacement vector  $\xi = (\xi_r, \xi_h \partial / \partial \theta, \xi_h \partial / \sin \theta \partial \phi) Y_l^m(\theta, \phi) e^{i\sigma t}$  and the relation  $\mathbf{v} = i\sigma \xi$ , each energy term is reduced after some manipulations in what follows,

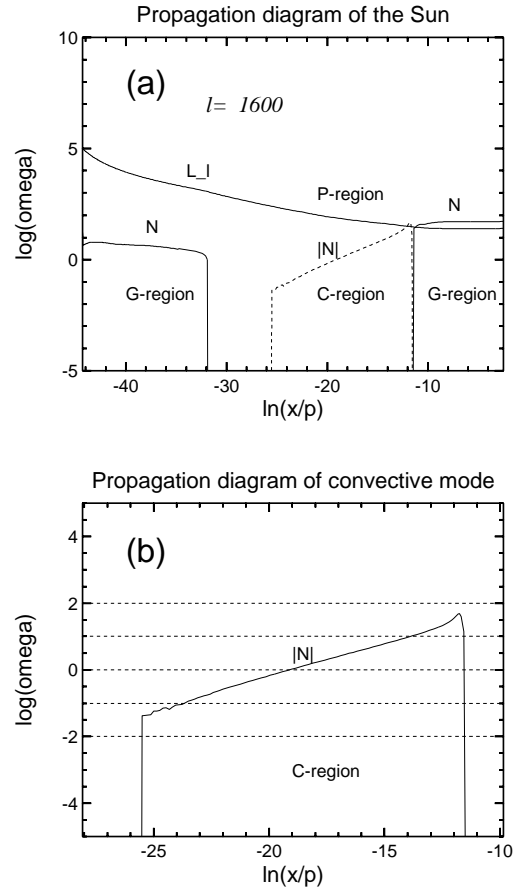


**Fig. 1.** (a): The propagation diagram of the Sun. Abscissa is  $\ln(x/p)$ , where  $x$  is fractional radius of the Sun ( $r/R_{\odot}$ ) and  $p$  is pressure. The left end is the center of the solar core and the right end is the solar surface. Ordinate is non-dimensional frequency ( $\omega = \sigma/\sqrt{GM_{\odot}/R_{\odot}^3}$ ). Solid lines designated by  $L_l$  and  $N$  indicate Lamb frequency and Brunt-Väisälä frequency, respectively. p-mode and g-mode can propagate in the P-region and in the G-region, respectively.  $|N|$  is given by dashed line. Convective mode ( $g^-$ -mode) is confined in the C-region.

(b): Enlarged propagation diagram of convective mode. A group of horizontal broken lines is a good indicator to see a confined region for a given  $\omega_l$  of  $g^-$ -mode.

Alt text: Two line graphs. In the upper panel, x axis shows radial position of the Sun. y axis shows non-dimensional frequency measured with free fall timescale of the Sun. The upper panel describes in what region a mode is trapped. In the lower panel, C-region is enlarged

$$e_k = \frac{1}{2} \mathbf{v}^2 = \frac{1}{2} \left\{ (i\sigma\xi_r)^2 + \ell(\ell+1) (i\sigma\xi_h)^2 \right\}, \quad (6)$$

$$e_p = \frac{1}{2} \left( \frac{p'}{\rho c} \right)^2, \quad (7)$$

$$e_g = \frac{1}{2} N^2 \left( \xi_r - v_T \frac{g}{N^2} \frac{\delta S}{C_p} \right)^2, \quad (8)$$

$$e_s = -\frac{1}{2} N^2 \frac{\nabla}{\nabla_{ad}} \left( v_T \frac{g}{N^2} \frac{\delta S}{C_p} \right)^2. \quad (9)$$

Here the kinetic energy  $e_k$  is divided into radial component  $e_{kr}$  (the first term of Eq. (6)) and horizontal one  $e_{kh}$  (the second term), and then  $e_k = e_{kr} + e_{kh}$ . Here we call  $e_p$ ,  $e_g$ , and  $e_s$  as acoustic energy, gravity energy, and entropy energy, respectively. We also define the integrated energy  $E_k$ ,  $E_{kr}$ ,  $E_{kh}$ ,  $E_p$ ,  $E_g$ , and  $E_s$  over the relevant region for the corresponding energies per unit mass, (i.e.,  $E_k = \int e_k dM_r, \dots$ , etc.).

$e_k$  is the kinetic energy of wave (or motion) and the other terms represent the potential energies corresponding to the restoring forces. When  $e_p$  is dominant (i.e., p-mode), its wave energy is equi-partitioned into kinetic energy  $e_k$  and acoustic energy  $e_p$ . Provided that  $e_g$  is dominant in the adiabatic case (i.e.,  $\delta S = 0$ ), the internal gravity mode ( $N^2 > 0$ ; g-mode) or the convective mode ( $N^2 < 0$ ;  $g^-$ -mode) appears. In the former case, the gravity energy  $e_g$  is potential energy for the internal gravity wave. In the latter case, the energy  $e_g$  becomes the source term for convective mode ( $g^-$ -mode).

In case of  $\delta S \neq 0$ , the entropy energy  $e_s$  appears. When the term in the square bracket in  $e_s$  is small enough comparing with the first term in the square bracket of  $e_g$ , the argument for g-mode or  $g^-$ -mode is not so different from that of the adiabatic case mentioned above. The effect of entropy energy  $e_s$  is comparatively small.

When the second term in the square bracket in  $e_g$  dominates over the radial displacement ( $\xi_r$ ), the relation  $e_s \approx -\nabla/\nabla_{ad} e_g$  is realized. As a factor  $\nabla/\nabla_{ad} \sim 1$  in order of magnitude in the relevant region, it may suggest that they have alternate roles, that is, when one plays a role of source term, the other plays a role of potential energy, and vice versa. The discussion for g-mode or  $g^-$ -mode is absolutely different from that of the adiabatic case. We will discuss the meaning of these terms in more detail in non-adiabatic analysis.

### 2.3 Convective mode

Judging from the position of C-region in Fig.1(a), we set the integration region to  $[-28.0, -2.5]$  in  $\ln(x/p)$ . Here the convective modes (the fundamental mode  $g_0^-$  and three overtones  $g_1^-$ ,  $g_2^-$ , and  $g_3^-$ ) are calculated for each  $\ell$ , (i.e.  $\ell = 1, 2, 10, 100, 200, 400, 800, 1600, 3200, 6400, 12000$ , and  $24000$ ). The results are summarized in Fig. 2, in which non-dimensional growth rate  $\omega_l = \sigma_l / \sqrt{GM_\odot/R_\odot^3}$  is plotted.

In this figure, one straight line with slope 1 running through a point of  $g_0^-$ -mode for  $\ell = 1$  is drawn. The points for  $g_0^-$ -mode fit well in the lower  $\ell$  region to this line. It is easily derived from Eq. (4) that  $\sigma_l^2$  is proportional to  $\ell(\ell+1)$  in case of  $\sigma_l^2 \ll L_l^2, |N|^2$ , which was already pointed out by Hart (1973). It can be also applicable to growth rates of other overtones. But they gradually leaves this line towards larger  $\ell$  and is saturated because the condition of  $\sigma_l < |N|$  should be satisfied.

The radial displacement ( $\xi_r/r$ ) (solid line) and the horizontal one ( $\sqrt{\ell(\ell+1)}\xi_h/r$ ) (broken line) for  $g_0^-$ -mode and  $g_2^-$ -mode with  $\ell = 6400$  in the upper panels of Fig. 3, respectively. The radial

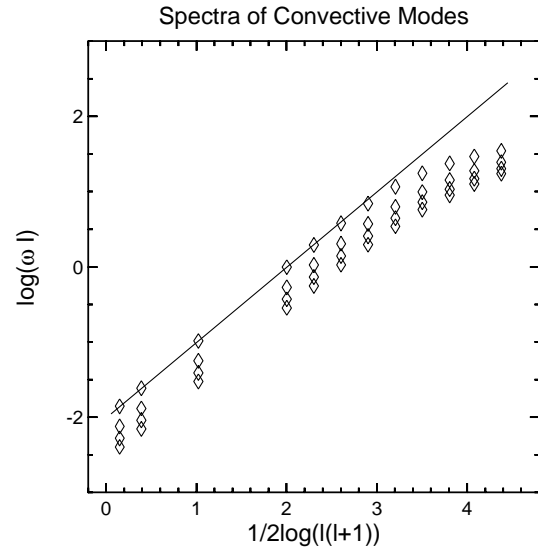


**Fig. 2.** The relation of growth rate  $\omega_l$  with spherical harmonics index  $\ell$  is shown. The growth rates of  $g_0^-$ ,  $g_1^-$ ,  $g_2^-$ , and  $g_3^-$ -mode are plotted for each  $\ell$  from top to bottom, respectively. One straight line with slope 1 runs through the growth rate of  $g_0^-$ -mode for  $\ell=1$ .

Alt text: x axis shows logarithm of spherical harmonics indicator  $\ell$ . y axis shows logarithm of growth rate of a mode.

distributions of energies ( $e_{kr}$ ,  $e_{kh}$ ,  $e_p$ , and  $e_g$ ) are also shown in the lower panels of Fig. 3. It should be noted here that the absolute values of energies are plotted, regardless of their signs.

We can see from "propagation diagram" of convective mode in Fig. 1(b) that the radial and the horizontal displacements for  $g_0^-$ -mode and  $g_2^-$ -mode are well confined between intersected points in C-region by horizontal lines of their growth rates  $\omega_l$ , respectively.

From the upper panel of Fig. 3(a) ( $g_0^-$ -mode), convective motion in a box-like cell cut off by top and bottom boundaries, and vertical boundaries specified by indices  $(\ell, m)$  of the spherical harmonics  $Y_l^m(\theta, \phi)$  is easily imagined. A peak of radial displacement (solid line) corresponds to zero point of the horizontal displacement (broken line). At both feet of the radial displacement, the local minimum and maximum of horizontal displacement appear. These features suggest circular motion of a gas element between the present cell and a neighboring cell. In addition to this, a peak of  $e_{kr}$  of  $g_0^-$ -mode corresponds to the local minimum of  $e_{kh}$  as shown in the lower panel of Fig. 3(a). This fact also supports this interpretation.

In Table 1, growth rate  $\omega_l$ , radial component  $E_{kr}$  and horizontal component  $E_{kh}$  of the total kinetic energy  $E_k$ , the total acoustic potential energy  $E_p$ , and the total gravity energy  $E_g$  are given for four modes, where all energies are normalized by  $E_k$ . Here the magnitude of  $E_k$  and  $E_g$  is almost same but with opposite sign for all modes. This comes from the fact that time derivative of wave energy  $e_w$  is zero owing to the adiabaticity. Then, the gravity energy  $E_g$  is transferred into the kinetic energy  $E_k$  and convective motion monotonically grows.

One important point is the distribution of gravity energy  $e_g$  shown by solid line with open circle in the lower panels of Fig. 3.  $g_0^-$ - and  $g_2^-$ -mode have one bump and three bumps in their distributions, respectively, which corresponds to number of nodes for each eigenfunction shown in the upper panels of Fig. 3. The radial displacement  $\xi_r$  is alone included in the square bracket of the

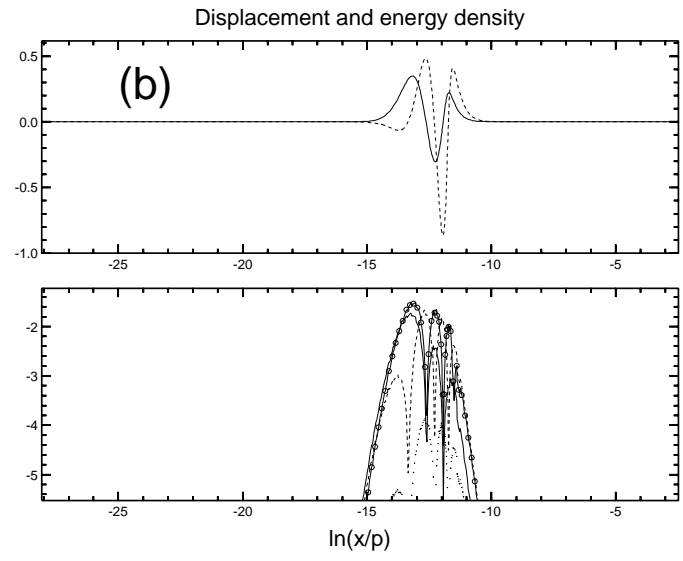
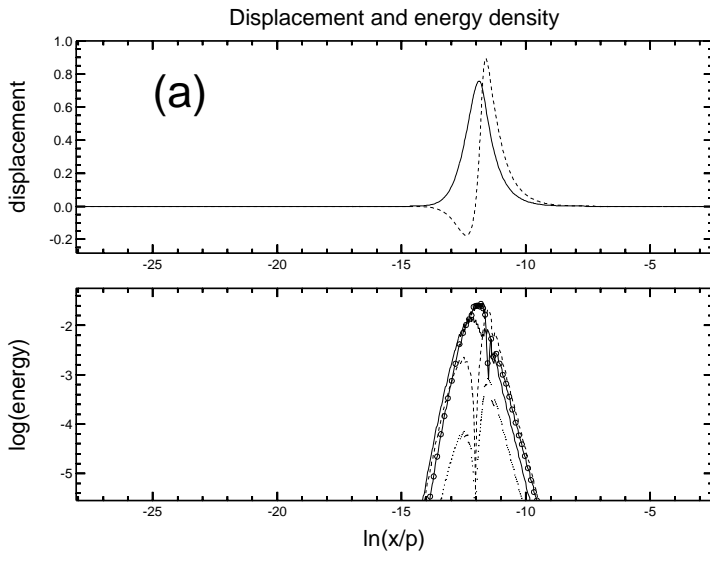


**Fig. 3.** (a): Upper panel shows displacement  $\xi_r/r$  (solid line) and  $\sqrt{l(l+1)}\xi_h/r$  (broken line) for  $g_0^-$ -mode with  $\ell = 6400$ . In lower panel, radial distribution of energies  $e_{kr}$  (solid line),  $e_{kh}$  (broken line),  $e_p$  (dotted line), and  $e_g$  (solid line with  $\circ$ ). The abscissa is  $\ln(x/p)$  and the ordinate is arbitrary. (b): The same plot as in figure (a) for  $g_2^-$ -mode with  $\ell = 6400$ .  
 Alt text: The left panel shows how radial displacement and potential energies of fundamental convective mode behaves in the radial direction of the Sun. x axis shows radial position of the Sun. y axis in the upper panel shows arbitrary unit. In the lower panel, logarithm of energy. The right panel shows the same line graph for the second overtone mode.

**Table 1.** Characteristics of  $g_0^-$ ,  $g_1^-$ ,  $g_2^-$ , and  $g_3^-$ -mode with  $\ell = 6400$  are given.  $E_{kr}$  and  $E_{kh}$  are radial and horizontal component of kinetic energy  $E_k$ , respectively. All energies are normalized by  $E_k$ .

Mode	$\omega_I$	$E_{kr}$	$E_{kh}$	$E_p$	$E_g$
$g_0^-$	-23.7	0.618	0.382	0.015	-1.020
$g_1^-$	-14.2	0.518	0.482	0.006	-1.006
$g_2^-$	-10.8	0.459	0.541	0.004	-1.004
$g_3^-$	-8.93	0.417	0.583	0.003	-1.003

gravity energy  $e_g$ .

### 3 Non-adiabatic analysis

The basic equations for non-adiabatic nonradial oscillations given by Ando & Osaki (1975) are used, in which Lagrangian perturbation of the divergence of convective flux is neglected (i.e.,  $\delta(\nabla \cdot \mathbf{F}_c) = 0$ ). The derivation of these basic equations is described in detail in the Appendix 1 of Ando & Osaki (1975). The same boundary conditions are employed except for the outer mechanical boundary condition.

As shown in the propagation diagram (Fig. 1), an eigenfunction with  $\omega_R \neq 0$  and higher  $\ell$  can propagate as a  $g$ -mode in the outer G-region and run away from the surface. So the zero boundary condition  $\delta P = 0$  is set as a mechanical boundary condition. The diffusion approximation of radiation transfer is also adopted as the thermal conduction. To compare with the adiabatic analysis, the case of  $\ell = 6400$  is calculated here. Integration region is limited to  $\ln(x/p) = [-28.0, -8.0]$ . The inner and the outer boundaries are selected to avoid mixed mode with  $g$ -mode in the G-regions (see Fig. 1(a)), because we concentrate on examination of properties of

convective mode. As shown later in Figs. 4 and 5, an eigenfunction of convective mode is, in fact, well trapped in C-region.

Shibahashi & Osaki (1981) showed that a mode with unusually large growth rate ( $|\omega_I| \sim \omega_R$ ) tends to a convective mode in the adiabatic limit. They replace the coefficient  $C_2$  in the basic equations by  $\alpha C_2$ . Here  $C_2$  is related with the ratio of local thermal time scale to dynamical time scale such as  $\tau_{th}/\tau_{dyn} = |\omega|C_2/V$  [i.e., equation (13) in Shibahashi & Osaki (1981)], where  $V$  is homologous invariant ( $-d \ln P / d \ln r$ ). By changing a parameter  $\alpha$ , they artificially change the degree of non-adiabaticity. For instance,  $\alpha = 0$  corresponds to the extreme non-adiabaticity (i.e., isothermal perturbation). In the limit of  $\alpha \rightarrow \infty$ , a perturbation behaves almost adiabatically. Now we calculate convective modes for three cases ( $\alpha = 1.0, 0.1, 0.01$ ). The results are summarized in Table 2.

#### 3.1 Monotonically growing convective mode

All modes with  $\omega_R = 0.00$  grow monotonically as shown in Table 2, although growth rates are reduced comparing with adiabatic case owing to the appearance of entropy perturbation ( $\delta S$ ) in  $e_g$  (i.e. Eq. (8)). The behaviors of  $g_0^-$ - and  $g_2^-$ -mode with  $\alpha = 1.00$  are presented in Fig. 4(a) and (b), respectively. Here the  $x$ -axis is enlarged to  $\ln(x/p) = [-20.0, -8.0]$  to see the detailed behaviors.  $dL/L$  indicates  $\delta L_{rad,r}/L_s$ , where  $\delta L_{rad,r}$  and  $L_s$  are the perturbation of the radiative luminosity at radius  $r$  and the total luminosity of the sun, respectively. Concerning energies, their square terms are given in terms of the square of amplitude of complex value. Usually (quasi-adiabatic case) each energy term is calculated as its average over the period. But the average values have no meaning in case of  $|\omega_I| \sim \omega_R$ .

For both modes, the radial displacements and the distributions of  $e_{kr}$ ,  $e_{kh}$ , and  $e_g$  look like those of adiabatic cases as drawn in

**Table 2.** Characteristics of non-adiabatic convective modes,  $g_0^-$ ,  $g_1^-$ ,  $g_2^-$ , and  $g_3^-$ -mode with  $\ell = 6400$  are given for each non-adiabatic indicator  $\alpha = 1.0, 0.1, 0.01$ . The parameter  $(\alpha\tau_{th}/\tau_{dyn})_{pk}$  is a value at the peak of the distribution of  $e_S$ .  $E_{kr}$  and  $E_{kh}$  are radial and horizontal component of kinetic energy  $E_k$ , respectively. All energies are normalized by  $E_k$ .

Mode	$\omega_R$	$\omega_I$	$(\alpha\tau_{th}/\tau_{dyn})_{pk}$	$E_{kr}$	$E_{kh}$	$E_p$	$E_g$	$E_S$
$\alpha = 1.0$								
$g_0^-$	0.00	-13.3	3.69	0.734	0.266	0.003	-1.889	0.434
$g_1^-$	0.00	-9.32	3.67	0.598	0.402	0.002	-1.882	0.352
$g_2^-$	0.00	-7.36	2.90	0.521	0.479	0.001	-2.140	0.442
$g_3^-$	0.00	-6.14	2.42	0.467	0.533	0.001	-2.584	0.628
$\alpha = 0.1$								
$g_0^-$	34.0	-12.0	1.42	0.629	0.371	0.029	-9.041	13.82
$g_1^-$	0.00	-7.62	0.63	0.640	0.360	0.001	-2.822	0.542
$g_2^-$	0.00	-6.03	0.50	0.553	0.447	0.001	-3.956	0.956
$g_3^-$	0.00	-5.02	0.60	0.494	0.506	0.001	-5.887	1.667
$\alpha = 0.01$								
$g_0^-$	48.5	-7.26	0.28	0.692	0.308	0.040	-11.92	18.20
$g_1^-$	13.1	-0.33	0.16	0.508	0.492	0.004	-9.118	7.147
$g_2^-$	9.42	-4.09	0.17	0.617	0.383	0.002	-9.278	5.610
$g_3^-$	0.00	-3.71	0.11	0.619	0.381	0.000	-17.90	5.000

Fig. 3. In fact, a mode can be still classified by number of nodes, which is also confirmed by number of bumps in the distributions of  $e_{kr}$ ,  $e_{kh}$ , and  $e_g$ . Besides, the imaginary parts of eigenfunctions are nearly zero, which means quasi-adiabatic condition. Higher order modes also have smaller growth rates. These features are common in modes with  $\omega_R = 0.00$ .

Most striking feature is an appearance of entropy energy distribution ( $e_S$ ) shown in Fig. 4. A peak of the distribution of  $e_S$  (solid line with x) corresponds to the steep rise of the perturbation of radiation luminosity  $dL/L$  around  $\ln(x/p) = -12.25$ , at which the divergence of radiation luminosity  $dL/L$  (i.e., thermal conduction) is maximum. In addition to this, the entropy energy  $e_S$  has only one conspicuous bump. This is the characteristics of  $e_S$  distribution in the non-adiabatic case. We now define the value of the ratio  $\alpha(\tau_{th}/\tau_{dyn})$  at a peak of  $e_S$  distribution denoted by  $(\alpha\tau_{th}/\tau_{dyn})_{pk}$  as a non-adiabaticity measure of  $e_S$  distribution. These values are given in Table 2.

For monotonically growing convective modes, it should be noted that a peak of  $e_S$  distribution is out of a main bulk of radial displacement, and thus the entropy energy  $e_S$  is distributed only in the partial area of the distributions of  $e_k = e_{kr} + e_{kh}$  and  $e_g$ . In fact,  $E_S$  is smaller than  $E_g$  by a factor of 4 or 5, and also smaller than  $E_k = E_{kr} + E_{kh}$  by a factor of 2 or 3, as shown in Table 2. This fact indicates that the first term ( $\xi_r$ ) in the square bracket of  $e_g$  dominates over the second term (entropy perturbation) as mentioned in the subsection 2.2. So the entropy energy  $e_S$  does not affect greatly the change of convective mode property, although growth rate is depressed.

### 3.2 Oscillatory convection

Table 2 shows that  $g_0^-$ -mode for  $\alpha = 0.1$  and  $g_0^-$ ,  $g_1^-$ , and  $g_2^-$ -mode for  $\alpha = 0.01$  become oscillatory (i.e.,  $\omega_R \neq 0$ ). In Fig. 5(a) and (b), the behaviors of  $g_0^-$ - and  $g_2^-$ -mode for  $\alpha = 0.01$  are presented, respectively.

They are totally different from the case of monotonically growing mode. They show only one bump in the radial displacement and the distributions of energies  $e_k$ ,  $e_g$ , and  $e_S$ . The distribution of entropy energy  $e_S$  (solid line with x) overlaps almost with that of  $e_g$  (solid line with  $\circ$ ), and these two energies prevail against the

displacement of kinetic energy  $e_k$ . It means that  $e_g$  is comparable in magnitude with  $e_S$ , although the two are different by a factor  $\nabla/\nabla_{ad}$ . In fact, Table 2 shows that  $E_S$  is almost comparable with  $E_g$  for oscillatory convective modes except for their signs and also they are considerably larger than  $E_{kr}$ . Therefore, gravity energy  $e_g$  acts as a source term of oscillatory convection and entropy energy  $e_S$  behaves like its potential energy, as stated in the subsection 2.2.

Oscillatory convection is no longer classified by the number of nodes, as the imaginary part of an eigenfunction is comparable with its real part. Instead, the real part of an eigenfrequency ( $\omega_R$ ) may be used as classification, as discussed later in the subsection 3.3.

Now what mechanism makes a monotonically growing convective mode oscillatory is raised. The most likely mechanism is considered to be Cowling mechanism (Cowling 1957). According to his physical picture, an element displaced upwards has higher temperature than the surrounding due to super-adiabaticity ( $\nabla > \nabla_{ad}$ ). The thermal loss through radiation in this phase forces the element to be cooler and denser in the following descending phase. The buoyancy accelerates the descending motion and brings the element deeper until the buoyant force pushes back an element owing to thermal gain through radiation from the surrounding. Although actual force is buoyant force, thermal conduction through radiation play a role of preventing an element from monotonically going upwards or downwards. Cowling's explanation is not inconsistent with our calculations and so it is considered to be the most promising mechanism at the moment.

### 3.3 Locus of $\omega$ with $\alpha$

We investigate how modes ( $g_0^-$ ,  $g_1^-$ ,  $g_2^-$ , and  $g_3^-$ ) change their features together with change of  $\alpha$ . In Fig. 6, the loci of eigenvalue ( $\omega$ ) are presented against  $\alpha$  for these modes along with  $C_3$  at a peak of entropy energy distribution ( $e_S$ ), where  $C_3$  is a fraction of radiation luminosity  $L_{rad}$  to the total luminosity  $L_s$  in the equilibrium model.

As for  $\omega_R$  ( $\diamond$ ), it becomes abruptly non-zero ( $\omega_R \neq 0$ ) at a certain  $\alpha$  during decrease of  $\alpha$  from  $10^2$  to  $10^{-10}$ , and thereafter keeps almost the same value. Once the thermal conduction through radiation makes a convective mode oscillatory, it does not affect much

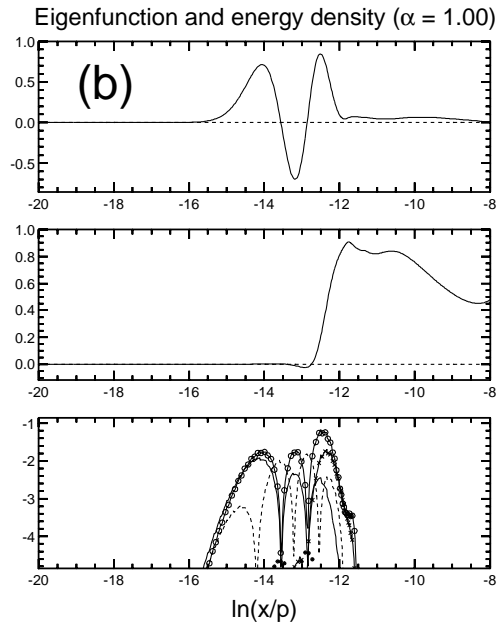
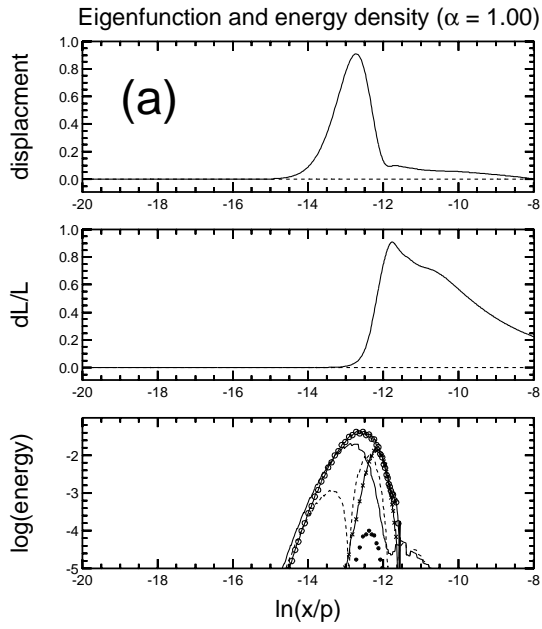


**Fig. 4.** (a): Non-adiabatic displacement, luminosity perturbation, and energy density of  $g_0^-$ -mode with  $\ell = 6400$  for  $\alpha = 1.0$ . Solid and broken lines in the upper panel indicate the real part and the imaginary part of radial displacement, respectively. Middle panel shows the luminosity perturbation, where  $(dL/L)$  means  $dL_{rad}/L_s$ . In the lower panel, a line with mark (x) presents the distribution of entropy energy  $e_s$ . The others are the same as in Fig. 3. (b): Non-adiabatic displacement, luminosity perturbation, and energy density distribution for  $g_2^-$ -mode. Alt text: Two line graphs. These graphs show the behaviors of monotonically growing convective modes.

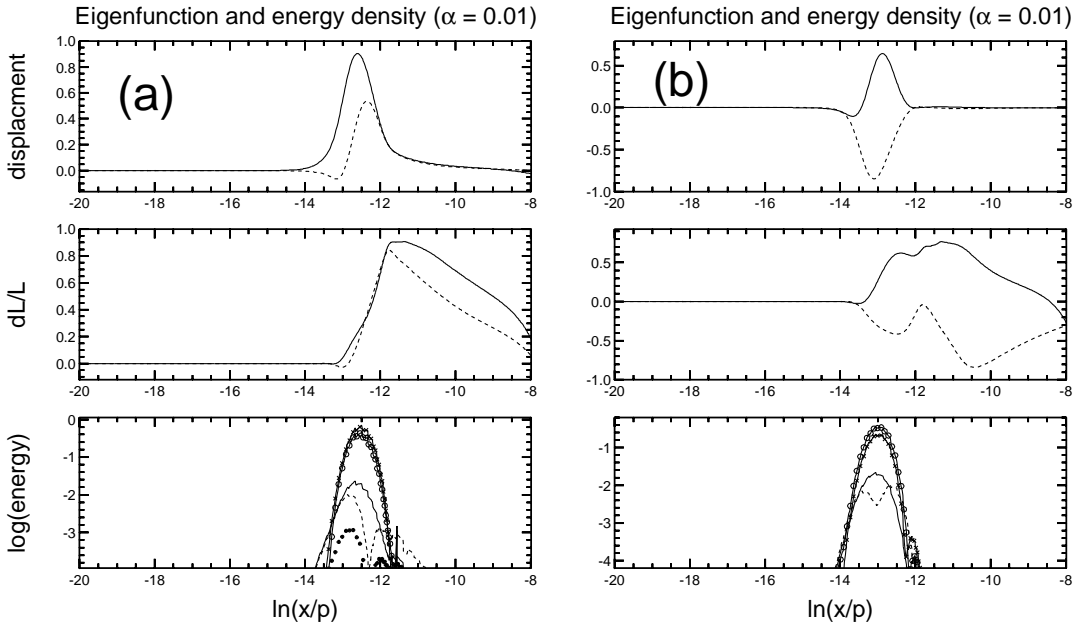


**Fig. 5.** (a): Non-adiabatic displacement and energy density of  $g_0^-$ -mode with  $\ell = 6400$  for  $\alpha = 0.01$ . Solid and broken lines in the upper panel indicate the real part and the imaginary part of radial displacement, respectively. Middle panel shows the luminosity perturbation ( $dL/L$ ). In the lower panel, a line with mark (x) presents the distribution of entropy energy  $e_S$ .  
(b): Non-adiabatic displacement, luminosity perturbation, and energy density distribution for  $g_2^-$ -mode.  
Alt text: Two line graphs. These graphs show the behaviors of oscillatory convection.

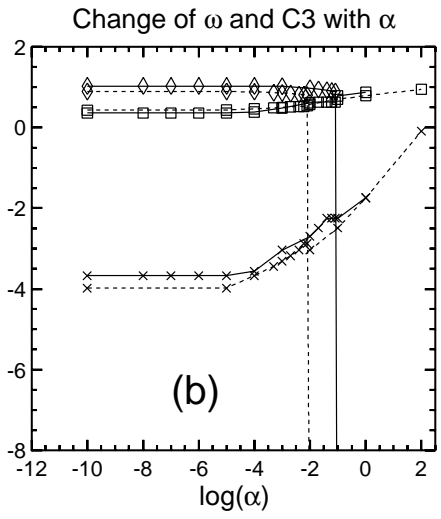
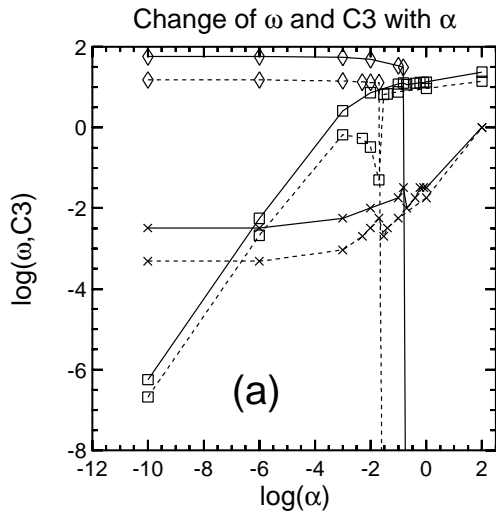


**Fig. 6.** (a): The changes of  $\omega_R$  are indicated by a solid line and a broken line with ( $\diamond$ ) for  $g_0^-$ - and  $g_1^-$ -mode, respectively. The changes of  $\omega_I$  are also drawn by a solid line and a broken line with ( $\square$ ). The lines with ( $\times$ ) show  $C_3$  value (i.e.:  $L_{rad}/L_s$ ) at a peak of  $e_S$  distribution for both modes. (b): The same explanation for  $g_2^-$ - and  $g_3^-$ -mode.

Alt text: Two line graphs. These graphs describe change of eigenfrequencies with the degree of non-adiabaticity.

the frequency itself. It is a very interesting feature, since oscillatory convection can be classified by its frequency.

Concerning  $\omega_I$  ( $\square$ ), it changes in the two ways. In Fig. 6(a) ( $g_0^-$  and  $g_1^-$ ),  $\omega_I$  is proportional to  $\alpha$  in the range of  $\alpha < 10^{-3}$ . On the other hand, it runs horizontally with  $\alpha$  as shown in Fig. 6(b) ( $g_2^-$  and  $g_3^-$ ), although it drops a little bit from the adiabatic value. Now we pay an attention to the behavior of  $C_3$ , which is the another coefficient  $C_3$  in the energy equation (11) given in Ando & Osaki (1975) other than  $C_2$ .  $C_3$  is a fraction of radiation luminosity ( $L_{rad}$ ) to the total luminosity ( $L_s$ ). The value of  $C_3$  at a peak of entropy energy distribution  $e_S$  is plotted for each mode by solid lines with ( $\times$ ) in both figures.  $C_3$  values in Fig. 6(b) are less than those in Fig. 6(a). We wonder that this fact might explain the different behavior in  $\omega_I$ . That is, when  $C_3$  value is less than a certain value, the thermal conduction through radiation contributing to both of  $e_S$  and  $e_g$  may be quenched to keep  $\omega_I$ . On the other hand, for the moderate  $C_3$  values, it may be effective to reduce  $\omega_I$ . Further examination should be stopped here, because a simple numerical experiment with use of  $C_3$  is inappropriate owing to its close relation with  $N^2$ -curve through the mixing length theory.

### 3.4 Application to the present Sun

As shown in Table 2, an oscillatory convection comes out when the parameter  $(\alpha\tau_{th}/\tau_{dyn})_{pk}$  is less than about 1.0. Then, we are aware of a possibility that a monotonically growing convective mode becomes oscillatory even in the present Sun. For smaller  $\ell$ ,  $\omega_I$  of a convective mode decreases as shown in Fig. 2, and the above parameter approaches about one.

For example, the behavior of eigenvalue with change of  $\ell$  is summarized for  $g_0^-$ -mode in Fig. 7. As  $\ell$  decreases from 1600, oscillatory convection appears abruptly around  $\ell = 1200$ , and then both of  $\omega_R$  and  $\omega_I$  decrease. In the oscillatory phase, the fact that the distribution of  $e_g$  overlaps almost with that of  $e_S$  is unchangeable.

But it should be noted that when  $\omega_R$  for  $g_0^-$ -mode is less than

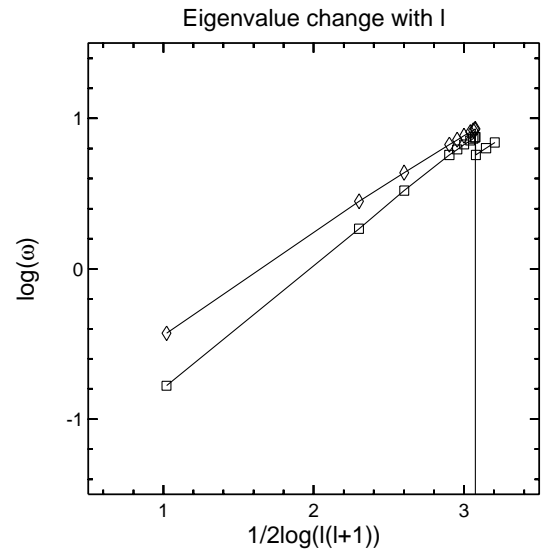


**Fig. 7.** Eigenvalue change with  $\ell$  for  $g_0^-$ -mode. It becomes oscillatory around  $\ell=1200$ .

Alt text: One line graph. This graph shows eigenfrequencies with spherical harmonics index  $\ell$ .

a peak of the inner  $G$ -region (about 6), it might become a mixed mode with a conventional  $g$ -mode. In this case, the careful analysis should be required. But it is beyond the present study, and we stop here.

## 4 Summary and discussion

In the adiabatic case, the "propagation diagram" for convective modes is introduced based on the local dispersion relation with  $\omega_I$ , which is useful to see the trapped region of convective modes. Any

eigenfunction of convective mode is well confined in C-region, which is very similar to the usual wave like  $p$ -mode or  $g$ -mode. It is also confirmed that eigenvalue  $\omega_l$  is proportional to  $\sqrt{\ell(\ell+1)}$ , as pointed out by Hart (1973).

As for non-adiabatic case, the systematic analysis of convective modes with  $\ell = 6400$  is carried out for three non-adiabatic indicators (i.e.,  $\alpha = 1.0, 0.1, \text{ and } 0.01$ ). For  $\alpha = 1.0$ , the convective modes are not so different in eigenfunction ( $\xi_r$ ) and energy distributions ( $e_k, e_g$ ) from those of the adiabatic convective modes. The entropy energy  $e_S$  plays only a role of the reduction of growth rate.

For smaller  $\alpha$ , a monotonically growing convective mode becomes abruptly oscillatory convection when the ratio  $(\alpha\tau_{th}/\tau_{dyn})_{pk}$  of local thermal time scale to dynamical time scale at a peak of entropy energy distribution  $e_S$  is less than about 1.0. Concerning an oscillatory convection, the situation is totally different from that of a monotonically growing convective mode. It shows only one bump in the radial displacement  $\xi_r$  and the energy distributions of energies  $e_k, e_g$ , and  $e_S$ . The distribution of entropy energy  $e_S$  almost overlap with the distribution of gravity energy  $e_g$ . At the same time, the thermal conduction through radiation is almost maximum around a peak of the distribution of entropy energy  $e_S$ . The entropy energy  $e_S$  seems to act as the potential energy for oscillatory convection. The mechanism of making a convective mode oscillatory may be explained by the Cowling mechanism proposed by Cowling (1957). Extending this notion, we also show the existence of oscillatory convection for  $\ell < 1200$  in the present Sun.

Through our systematic analysis, we can understand the role of the gravity energy  $e_g$  and the entropy energy  $e_S$  in the following. When  $N^2 < 0$ , the entropy energy  $e_S$  is considered to play a role of the potential energy for oscillatory convection, and the gravity energy  $e_g$  is source. On the other hand, in case of  $N^2 > 0$  the gravity energy  $e_g$  is the potential energy for  $g$ -mode, and the entropy energy  $e_S$  is source. Therefore, the problem of the overstable convection under the stabilized medium discussed by Cowling (1957) and Kato (1966) might correspond to the latter case.

In this work, the interaction of linear convective mode with convective motion in the equilibrium state has been neglected. It is not clear at the moment whether such an interaction has crucial impact on our result or not. We anticipate that such a difficult problem will be solved in the future.

## Acknowledgements

I would like to thank the referee for improving the paper with his helpful comments. I am also grateful to National Astronomical Observatory of Japan (NAOJ) for their financial support.

## References

- Ando H., Osaki Y., 1975, PASJ, 27, 581  
 Cowling T., 1957, Magnetohydrodynamics. Interscience Tract, Inc., New York  
 Hart M. H., 1973, ApJ, 184, 587  
 Kato S., 1966, PASJ, 18, 374  
 Latter H. N., 2016, MNRAS, 455, 2608  
 Osaki Y., 1975, PASJ, 27, 237  
 Paczyński B., 1969, Acta Astron., 19, 1  
 Saio H., 2011, MNRAS, 412, 1814  
 Saio H., Wood P. R., Takayama M., Ita Y., 2015, MNRAS, 452, 3863  
 Shibahashi H., Osaki Y., 1981, PASJ, 33, 427  
 Unno W., Osaki Y., Ando H., Saio H., Shibahashi H., 1989, NONRADIAL OSCILLATIONS OF STARS, second edn. University of Tokyo Press, Tokyo